

First observation of two hyperfine transitions in antiprotonic ${}^3\text{He}$

S.Friedreich^a, D. Barna^{b,c}, F. Caspers^d, A. Dax^b, R.S. Hayano^b, M. Hori^{b,e}, D. Horváth^{c,f}, B. Juhász^a, T. Kobayashi^b, O. Massiczek^a, A. Sótér^e, K. Todoroki^b, E. Widmann^a, J. Zmeskal^a

^a*Stefan Meyer Institute for Subatomic Physics, Austrian Academy of Sciences, Boltzmanngasse 3, A-1090 Vienna, Austria*

^b*Department of Physics, University of Tokyo, 7-3-1 Hongo, Bunkyo-ku, Tokyo 113-0033, Japan*

^c*KFKI Research Institute for Particle and Nuclear Physics, H-1525 Budapest, PO Box 49, Hungary*

^d*CERN, CH-1211 Geneva, Switzerland*

^e*Max-Planck-Institut für Quantenoptik, Hans-Kopfermann-Strasse 1, D-85748 Garching, Germany*

^f*Institute of Nuclear Research of the Hungarian Academy of Sciences, H-4001 Debrecen, PO Box 51, Hungary*

Abstract

We report on the first experimental results for microwave spectroscopy of the hyperfine structure of $\bar{\text{p}}^3\text{He}^+$. Due to the helium nuclear spin, $\bar{\text{p}}^3\text{He}^+$ has a more complex hyperfine structure than $\bar{\text{p}}^4\text{He}^+$ which has already been studied before. Thus a comparison between theoretical calculations and the experimental results will provide a more stringent test of the three-body quantum electrodynamics (QED) theory. Two out of four super-super-hyperfine (SSHF) transition lines of the $(n, L) = (36, 34)$ state were observed. The measured frequencies of the individual transitions are 11.12559(14) GHz and 11.15839(18) GHz, less than 1 MHz higher than the current theoretical values, but still within their estimated errors. Although the experimental uncertainty for the difference of these frequencies is still very large as compared to that of theory, its measured value agrees with theoretical calculations. This difference is important because it is proportional to the magnetic moment of the antiproton.

Keywords: antiprotonic helium, microwave spectroscopy, hyperfine structure, three-body QED

PACS: 36.10.-k, 32.10.Fn, 33.40.+f

1. Introduction

It was observed for the first time at KEK in Japan in 1991 [1] that antiprotons stopped in helium can survive for several microseconds. If an antiproton is approaching a helium atom at its ionization energy (24.6 eV) or below, the antiproton can eject one of the two electrons from the ground state of the helium atom, replace it and thus get captured. This exotic, metastable three-body *antiprotonic helium*, i.e. $\bar{\text{p}}\text{He}^+$, consists of one electron in the ground state, the helium nucleus and the antiproton [2–4]. The atoms occupy circular states with L close to n , where L is the angular momentum quantum number and n the principal quantum number. The electron remains in the ground state. The antiproton is, due to its high mass, most likely to be captured into states with high angular momentum, i.e. $n = n_0 \equiv \sqrt{M^*/m_e} \sim 38$, M^* being the reduced mass of the system. About 97% of these exotic atoms find themselves in states domi-

nated by Auger decay and ionize within a few nanoseconds because of the Auger excitation of the electron. Afterwards the remaining antiprotonic helium ion undergoes Stark mixing due the electric field of the surrounding helium atoms. The antiprotons then annihilate within picoseconds with one of the nucleons of the helium nucleus because of the overlap of their wavefunctions. Only 3% of the antiprotonic helium atoms remain in metastable, radiative decay-dominated states. In this case, the change of orbital angular momentum in the Auger transition is large and thus Auger decay is suppressed. Consequently, these states are relatively long lived, having a lifetime of about 1-2 μs . This time window can be used to do microwave spectroscopy measurements.

2. Hyperfine structure of antiprotonic helium

The interaction of the magnetic moments of its constituting particles gives rise to a splitting of the $\bar{\text{p}}^3\text{He}^+$ energy levels. The coupling of the electron spin \vec{S}_e and the orbital angular momentum of the antiproton L leads

Email address: susanne.friedreich@oeaw.ac.at (S.Friedreich)

to the primary splitting of the state into a doublet structure, referred to as *hyperfine (HF) splitting*. The quantum number $\vec{F} = \vec{L} + \vec{S}_e$ defines the two substates as $F_+ = L + \frac{1}{2}$ and $F_- = L - \frac{1}{2}$. The non-zero spin of the ${}^3\text{He}$ nucleus causes a further, so-called *super-hyperfine (SHF) splitting*, which can be characterized by the quantum number $\vec{G} = \vec{F} + \vec{S}_h = \vec{L} + \vec{S}_e + \vec{S}_h$, where \vec{S}_h is the spin of the helium nucleus. This results in four SHF substates. At last, the spin-orbit interaction of the antiproton orbital angular momentum and antiproton spin $\vec{S}_{\bar{p}}$ in combination with the contact spin-spin and the tensor spin-spin interactions between the particles result in a further splitting of the SHF substates into eight substates – as illustrated in Fig. 1 –, which we call *super-super-hyperfine (SSHF) splitting*. This octuplet structure can be described by the quantum number $\vec{J} = \vec{G} + \vec{S}_{\bar{p}} = \vec{L} + \vec{S}_e + \vec{S}_h + \vec{S}_{\bar{p}}$. Even though the magnetic moment of the antiproton is larger than that of the ${}^3\text{He}$ nucleus, the former has a smaller overlap with the electron cloud, therefore it creates a smaller splitting.

In $\bar{\text{p}}^4\text{He}^+$, however, where the ${}^4\text{He}$ nucleus has zero spin, only a quadruplet structure is present. The hyperfine structure of the $(n, L) = (37, 35)$ state of $\bar{\text{p}}^4\text{He}^+$ was already extensively studied. Through comparison of the experimental results to state-of-the-art three-body QED calculations a new experimental value for the spin magnetic moment of the antiproton was obtained as $\mu_s^{\bar{p}} = 2.7862(83)\mu_N$ [5], where μ_N is the nuclear magneton. This is more precise than the previous measurement by Kreissl et al. [6]. The agreement with $\mu_s^{\bar{p}}$ was within 0.24% [7, 8].

New microwave spectroscopy measurements with $\bar{\text{p}}^3\text{He}^+$ were started, studying the state $(n, L) = (36, 34)$. It was the first attempt to measure the microwave transition frequencies of antiprotonic ${}^3\text{He}$. Transitions between the SSHF states can be induced by a magnetic field oscillating in the microwave frequency range. Due to technical limitations of the microwave input power, only the transitions which flip the spin of the electron can be measured. There are four such "allowed" SSHF transitions for the $(n, L) = (36, 34)$ state of $\bar{\text{p}}^3\text{He}^+$, of which we report on two:

$$\begin{aligned} \nu_{\text{HF}}^{--} : J^{---} = L - \frac{3}{2} &\longrightarrow J^{+--} = L - \frac{1}{2} \\ \nu_{\text{HF}}^{-+} : J^{--+} = L - \frac{1}{2} &\longrightarrow J^{++-} = L + \frac{1}{2} \end{aligned} \quad (1)$$

The interest in $\bar{\text{p}}^3\text{He}^+$ arose from its more complex structure due to the additional coupling of the nuclear spin with the antiproton orbital momentum. Such a

measurement will allow a more rigorous test of the theory. The theoretical calculations have been developed by two different groups [9–11]. The hyperfine structure for $\bar{\text{p}}^3\text{He}^+$ has been calculated by V. Korobov [12] with the most accurate variational wave functions.

3. Laser-microwave-laser spectroscopy

The experimental technique is a three-step process, referred to as *laser-microwave-laser spectroscopy* (Fig. 1). After antiprotonic helium is formed, the atoms in the hyperfine substates are in thermal equilibrium and the states are all equally populated. Therefore, at first a population asymmetry between the SSHF substates of the measured radiative decay state (n, L) needs to be created. This depopulation is induced by a short laser pulse which transfers the majority of the antiprotons from one of the HF states of the radiative decay-dominated, metastable parent state to the Auger decay-dominated, short-lived daughter state (f^+ transition in Fig. 1). The bandwidth of the laser is narrow enough so that the f^- transition is not excited. Therefore the antiprotons in the other HF state are not affected, which results in the desired population asymmetry. The antiprotons in the short-lived daughter state annihilate within a few nanoseconds. Afterwards, a microwave frequency pulse, tuned around the transition frequency between two SSHF ($\bar{\text{p}}^3\text{He}^+$) substates of the parent state, is applied to the antiprotonic helium atoms. If the microwave field is on resonance with one of the SSHF transitions, this will cause a population transfer and thus a partial refilling of one of the previously depopulated states. Then, a second laser pulse is applied again to the same transition (f^+) as before, which will again result in subsequent Auger decay of the transferred atoms and annihilation of the antiprotons. Thus, the number of annihilations after the second laser pulse will be larger if more antiprotons were transferred by the microwave pulse.

The annihilation decay products – primarily charged pions, but also electrons and positrons – resulting from the decay of the daughter state after the two laser pulses, are detected by two Cherenkov counters (see chapter 4). Prior to the first laser-induced population transfer a large annihilation peak (prompt) is caused by the majority of $\bar{\text{p}}\text{He}^+$ atoms which find themselves in Auger decay-dominated states and annihilate within picoseconds after formation. At later times, this peak exhibits an exponential tail due to $\bar{\text{p}}\text{He}^+$ atoms in the metastable states cascading more slowly towards the nucleus. This constitutes the background for the laser-induced annihilation signals. As mentioned above, the daughter state

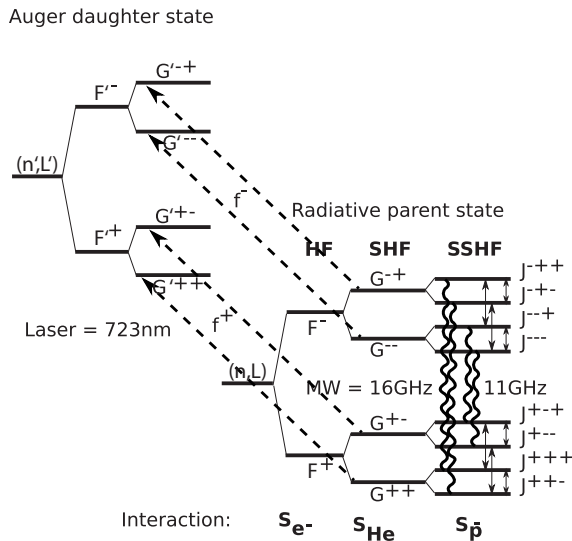


Figure 1: A schematic drawing of the laser-microwave-laser method. The dashed arrows indicate the laser transitions between the SHF levels of the radiative decay-dominated state $(n, L) = (36, 34)$ and the Auger decay-dominated state $(n', L) = (37, 33)$ of $\bar{p}^3\text{He}^+$. The wavy lines illustrate the microwave-induced transitions between the SSHF levels of the long-lived state.

130 has a very short lifetime of ~ 10 ns and thus the population transfer is indicated by a sharp annihilation peak against the background during the two laser pulses. The area under these peaks is proportional to the population transferred to the Auger decay-dominated state. This spectrum is called an *analogue delayed annihilation time spectrum* or ADATS. The spectrum with the two laser-induced peaks superimposed on the exponential tail are displayed in Fig. 2.

139 Since the intensity of the antiproton pulse fluctuates from shot to shot, the peaks must be normalised by the total intensity of the pulse (total). This ratio is referred to as *peak-to-total*. The peak-to-total (ptt) corresponds to the ratio of the peak area ($I(t_1)$ or $I(t_2)$) to the total area under the full spectrum, as displayed in Fig. 2. If the second laser annihilation peak is further normalised to the first one, the total cancels out. The frequencies of the two SSHF transitions can now be obtained as distinct lines by plotting $\frac{I(t_2)}{I(t_1)}$ as a function of the microwave frequency. The ratio $\frac{I(t_2)}{I(t_1)}$ is largely independent of the intensity and position of the antiproton beam. The height of the microwave spectrum lines depends on the time delay between the two laser pulses and collisional relaxation effects.

149 For these measurements the two pulsed lasers were

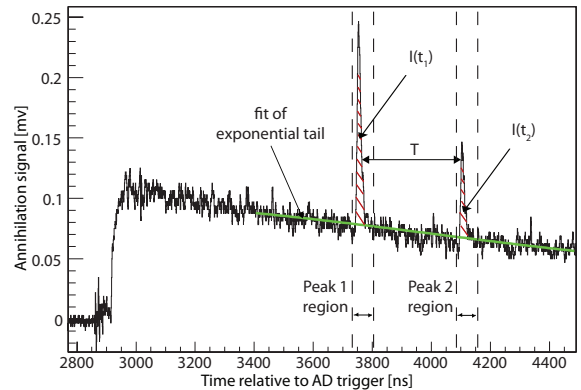


Figure 2: Part of the analog delayed annihilation time spectrum (ADATS) with the two laser-stimulated annihilation peaks against the exponential decaying background of the metastable cascade. T denotes the delay time between the two laser pulses. The photomultipliers are gated off during the initial \bar{p} pulse arrival [13]. Thus, the prompt peak is cut off and only the annihilations due to the metastable state depopulation are recorded.

155 fixed to a wavelength of 723.877 nm (see chapter 5),
 156 with a pulse length of 10-12 ns, to induce the f^+
 157 laser transition between the $(n, L) = (36, 34)$ and the
 158 $(n', L') = (37, 33)$ state. The laser power was in the
 159 range of 20-40 mJ/cm². There are several limitations
 160 to the choice of the measured state, such as availability
 161 of a laser source in the required frequency range or
 162 the splitting of the transitions between the HF states
 163 of the daughter and the parent state. The laser transi-
 164 tion between the $(n, L) = (36, 34)$ and the $(n', L') =$
 165 $(37, 33)$ state was chosen because it is easily stimulated
 166 and the primary population is large, thus leading to a
 167 large signal. The captured fraction of antiprotons for
 168 the measured metastable state $(n, L) = (36, 34)$ is $(3-$
 169 $4) \times 10^{-3}$ [14].

4. Experimental setup

170 The antiprotons for the experiment were provided by
 171 the AD (Antiproton Decelerator) at CERN [15], with a
 172 pulsed beam of $(1-3) \times 10^7$ antiprotons at an energy of
 173 5.3 MeV at a repetition rate of about 100 s. The parti-
 174 cles were stopped in a helium gas target, cooled down
 175 to a temperature of about 6 K. The usual gas pressure
 176 was in the range of 150-500 mbar. The gas target was
 177 a cylindrical chamber, which also acted as a microwave
 178 resonance cavity. In order to measure the annihilation
 179 decay products two Cherenkov counters were mounted
 180 around the target volume. The resulting photons are de-

181 tected by photomultipliers which are gated off during 233
 182 the initial \bar{p} pulse arrival [13]. The microwave pulse was 234
 183 synthesized by a vector network analyzer (VNA, Rhode 235
 184 & Schwarz ZVB20) and amplified by a travelling wave 236
 185 tube amplifier (TWTA, TMD PTC6358). A waveguide 237
 186 system then transmitted the microwave pulse of $\sim 20 \mu\text{s}$ 238
 187 to the cavity. Fig. 3 gives an overview of the central part 239
 188 of the setup. 240

189 The experimental method and the general design of 241
 190 the setup were the same as for $\bar{p}^4\text{He}^+$ [16]. How- 242
 191 ever, a new cryostat with compressor-based cooling 243
 192 system was built, which led to improvements of the 244
 193 operation and more efficient use of the measurement 245
 194 time [17]. The microwave cavity was now cooled 246
 195 directly by mounting it on a coldhead. Only the cavity 247
 196 was filled with the helium gas and by means of the 248
 197 coldhead cooled down to about 6 K. Liquid nitrogen 249
 198 and liquid helium were no longer needed for the cool- 250
 199 ing process. The temperature stabilization was much 251
 200 faster compared to the old system. The cryostat could be 252
 201 operated continuously and thus saved $\sim 10\%$ of beam- 253
 202 time previously needed for refilling of the cryogenic 254
 203 coolants. 255

204 Out of the four allowed SSHF transitions of the state 256
 205 $(n, L) = (36, 34)$ of $\bar{p}^3\text{He}^+$, two of them lie within 257
 206 32 MHz from each other. Therefore these two transi- 258
 207 tions can be measured with a single cavity with a reso- 259
 208 nance frequency of 11.14 GHz, which is in the middle 260
 209 between the two SSHF transition frequencies. For the 261
 210 other two transitions, another cavity with a resonance 262
 211 frequency of 16.13 GHz will be used in the future. 263

212 The cavity was built of brass, which has proven to 264
 213 be the optimum combination of machinability and ther- 265
 214 mal conductivity and is further unmagnetic. The central 266
 215 frequency of a cylindrical microwave cavity is defined 267
 216 by its dimensions – length l and radius r . The cavity 268
 217 used for the measurements of the 11 GHz transitions 269
 218 has a radius of 16.19 mm and a length of 26.16 mm.
 219 It is oriented in a way that the antiproton beam and the
 220 laser beam enter along the axis of the cavity. Two stain-
 221 less steel meshes (transmissibility $>90\%$, $250 \mu\text{m}$ thick,
 222 wire thickness 0.05 mm, wire distance 0.75 mm) on
 223 both faces of the cylinder confine the radio-frequency
 224 field inside the cavity, still allowing the laser and the
 225 antiprotons to enter the target.

226 Radius and length – and their ratio $(\frac{2r}{l})^2$ – also deter- 275
 227 mine which field modes can resonate inside the cavity 276
 228 and at which frequency. For this experiment the trans- 277
 229 verse magnetic mode TM_{110} for a cylindrical cavity has 278
 230 been chosen which is parallel to the axis of the cylindri- 279
 231 cal cavity and independent of the cavity length, i.e. on 280
 232 the direction of the antiproton beam. It is useful to have 281

233 a homogeneous field over a large range in the direction
 234 of the antiproton beam in order to be less sensitive to
 235 the stopping region of the antiprotons in the gas. It is
 236 also desirable that the field distribution is uniform over
 237 the region where the laser is applied – which is usually
 238 smaller than the diameter of the slowed down antiproton
 239 beam to achieve sufficient laser power density. Further,
 240 the size of the homogeneous resonating field in trans-
 241 verse direction to the beam should be comparable to the
 242 stopping distribution of the antiprotons.

A broad resonance of the cavity is necessary to allow
 scanning over a large enough frequency range in order
 to measure both SSHF transitions with the same cavity
 at an equal power level [16]. The field is measured with
 a small (~ 2 mm) pin antenna opposite to the wave-
 guide input. Thus, the power in the cavity was monitored
 and the input power adjusted for every frequency point,
 with a power fluctuation of $\sim 16\%$ over the frequency
 range. The only drawback is that considerably high in-
 put power, i.e. up to 200 W, might be required. To ob-
 tain a sufficiently broad resonance with a FWHM of at
 least 100 MHz the cavity is overcoupled to the wave-
 guide system through an iris, a rectangular aperture in
 the cavity. The iris of the 11 GHz target has a size of
 7×8 mm, the longer side in radial direction; this way
 the resonance width of the cavity was ~ 140 MHz. These
 are fixed parameters of the setup. When designing the
 target, the width of the resonance can be optimized by
 changing the iris dimensions – and consequently also
 the central frequency shifts, which can be readjusted
 by changing the radius. The length may also have to
 be adapted in order to exclude interferences with other
 field modes. In particular the iris size is crucial for a
 successful measurement since it may cause polarization
 degeneration of the mode in the cavity. The whole mi-
 crowave part of the setup was designed using the High
 Frequency Structure Simulator (HFSS) Software [18].

5. Results

First, a scan over the laser frequency range was done
 to determine the frequency offset and the splitting of
 the two HF lines (see Fig. 4) to ensure that only one
 of the two hyperfine levels of the $(n, L) = (36, 34)$
 state is depopulated by laser stimulation. The split-
 ting is $\Delta f = 1.72 \pm 0.03$ GHz, similar to the tran-
 sition at ~ 726.090 nm in $\bar{p}^4\text{He}^+$, with a splitting of
 $\Delta f = 1.75 \pm 0.01$ GHz. Due to the different SSHF en-
 ergy level spacings, one of the laser transition peaks has
 a lower amplitude and larger width. Each of these peaks
 consists of another two subpeaks, corresponding to tran-
 sitions from one SHF substate of the parent state to the

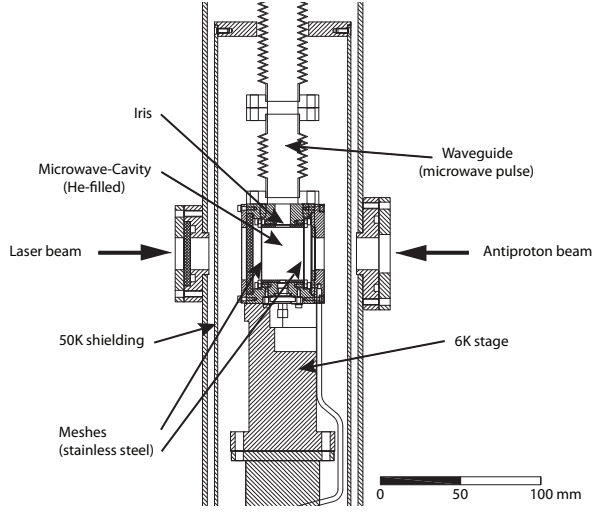


Figure 3: Drawing of the central part of the experimental setup, a cross-section of the cryostat.

282 same SHF substate of the daughter state. Two of the
 283 four SHF substates, respectively, are lying close enough
 284 to each other to have a frequency difference smaller than
 285 the laser linewidth (~ 100 MHz) and the Doppler width
 286 (~ 300 MHz) and can thus not be resolved while the
 287 other two lines have a splitting in the range of the broad-
 288 ening and thus result in a smaller and broader peak.

289 The measurements were all performed with a delay
 290 time T between the two lasers of 350 ns and a target
 291 pressure of 250 mbar. These parameters shall provide a
 292 first comparison with results in $\bar{p}^4\text{He}^+$. A study at dif-
 293 ferent laser delay times and target pressures is planned
 294 to be done in the future.

295 Two of the four allowed SSHF resonance transitions
 296 in $\bar{p}^3\text{He}^+$ could be observed. The scans of the two
 297 microwave-induced transitions are displayed in Fig. 5.
 298 They were both fitted with the function of their natural
 299 line shape. For a two-level system which is affected by
 300 an oscillating magnetic field for a time T the line shape
 301 is given by [19]

$$X(\omega) = \frac{|2b|^2}{|2b|^2 + (\omega_0 - \omega)^2} \times \sin^2 \left\{ \frac{1}{2} \left[|2b|^2 + (\omega_0 - \omega)^2 \right]^{\frac{1}{2}} T \right\}. \quad (2)$$

302 Here $X(\omega)$ is the probability that an atom is transferred
 303 from one HF state to the other, ω is the angular fre-
 304 quency of the magnetic field, and ω_0 is the angular fre-
 305 quency of the transition between the two energy levels.
 306 The parameter $b = \Omega/2$ is a time independent part of
 307 the transition matrix elements between two energy lev-

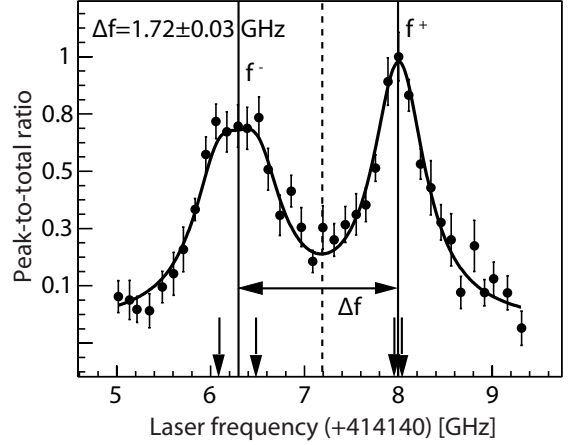


Figure 4: Laser resonance profile for the $(n, L) = (36, 34)$ state of $\bar{p}^3\text{He}^+$, displaying the two laser transitions f^+ and f^- between the HF states of the parent and the daughter state, at a target pressure of 250 mbar. The peaks are fitted with four Voigt functions referring to the four allowed E1 transitions between the SHF states of the parent state (refer to Fig. 1). The arrows indicate the corresponding theoretical transition frequencies.

308 els, with the Rabi frequency Ω . In the case of a com-
 309 plete π -pulse, one obtains $|b|T = \pi/2$. This is referred
 310 to as the optimum case, since together with $X(\omega) = 1$
 311 at resonance this gives the smallest width for the transi-
 312 tion line, $\Gamma = \frac{0.799}{T}$ [19]. The Fourier transform of the
 313 rectangular microwave pulse gives a lower limit for the
 314 transition line width.

315 From the fit, the frequencies for the measured ν_{HF}^{--} and
 316 ν_{HF}^{+-} transitions can be obtained. All relevant results are
 317 summarized in Table 1. For a pulse of length $T = 350$ ns
 318 the expected width is $\Gamma = 2.28$ MHz [19] which is
 319 roughly in agreement with the measurement. In order
 320 to determine the optimum power to induce an electron
 321 spin flip and thus the maximum population transfer be-
 322 tween two SSHF states, the signal was tested at sev-
 323 eral different microwave powers. The ν_{HF}^{--} transition
 324 was measured with a power of about 10 W and the ν_{HF}^{+-}
 325 transition at about 7.5 W, leading to an average oscil-
 326 lating magnetic field amplitude of $0.24(4) \times 10^{-4}$ T and
 327 $0.19(3) \times 10^{-4}$ T, respectively, inside the microwave cav-
 328 ity, calculated using the measured Q value and
 329 the theoretical formula for the magnetic field in a cylin-
 330 drical cavity. The Rabi frequency $\Omega_m = \frac{\mu_m B_0}{\hbar}$, with μ_m
 331 denoting the magnetic dipole moment, is dependent on
 332 the microwave power. The microwave power has to be
 333 chosen to achieve a complete π -pulse. Due to lack of
 334 time for more accurate power studies the two transitions

335 have been measured at only one power each, which are
 336 slightly different from each other. These measurements
 337 will have to be repeated with improved statistics.

338 There were also systematic effects which had to be
 339 considered. The largest influence was due to the shot-
 340 to-shot fluctuations of the antiproton beam. These ef-
 341 fects were reduced by normalising to the total intensity
 342 of the pulse and further normalising the second annihi-
 343 lation peak to the first one (refer to chapter 3). There-
 344 fore, mainly shot-to-shot fluctuations of the microwave
 345 power and deviations in the laser position and fluence
 346 from day to day – although considerably smaller – con-
 347 tributed to the error quoted in Table 1.

348

349 The experiment has been numerically simulated by
 350 solving the optical Bloch equations in order to estimate
 351 important measurement parameters, in particular the re-
 352 quired microwave power and the signal-to-noise-ratio.
 353 The Bloch equations describe the depopulation of states,
 354 in this experiment induced by laser light and microwave
 355 radiation and under the influence of collisional effects.
 356 For most parameters, such as microwave power, Q value
 357 and laser delay, the measured values were taken. The
 358 rates of collisional effects – inducing relaxations be-
 359 tween the SSHF substates – were obtained from adjust-
 360 ing the simulation to the experimental results for the $\bar{p}^4\text{He}^+$
 361 resonance, and they are comparable to the values for
 362 $\bar{p}^4\text{He}^+$. Fig. 5 shows the results of the simulations in
 363 comparison to the fitted measurement data. The numeri-
 364 cal simulations are explained in detail in [20].

365 The measured hyperfine transition frequencies agree
 366 with theory [12] within less than 1 MHz. The current
 367 precision of ~ 20 ppm is still worse than for the most re-
 368 cent results with $\bar{p}^4\text{He}^+$ which gave an error of 3 ppm
 369 for the individual transition lines [5]. Due to limitations
 370 in antiproton beam quality this precision for $\bar{p}^4\text{He}^+$
 371 is not likely to be improved anymore. However, it is also
 372 unlikely to achieve an error for $\bar{p}^3\text{He}^+$ as small as for
 373 $\bar{p}^4\text{He}^+$. There are eight instead of four SSHF energy lev-
 374 els in $\bar{p}^3\text{He}^+$ and thus the measured signal will be only
 375 about half of the signal obtained for $\bar{p}^4\text{He}^+$. Therefore,
 376 much higher statistics would be required.

377 A comparison of the theoretical values for the two
 378 SSHF transitions at 11 GHz with the measurement re-
 379 sults shows that there is a small shift in frequency to-
 380 wards higher values for both transitions. The frequency
 381 difference $\Delta v_{\text{th-exp}}$ between theory and experiment is
 382 ~ 0.6 MHz for ν_{HF}^- and ~ 0.7 MHz for ν_{HF}^+ respectively.
 383 According to V. Korobov, this discrepancy is most likely
 384 due to the theoretical limits of the Breit-Pauli approxi-

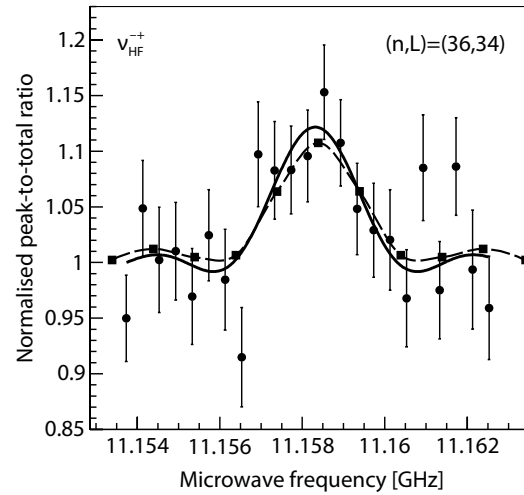
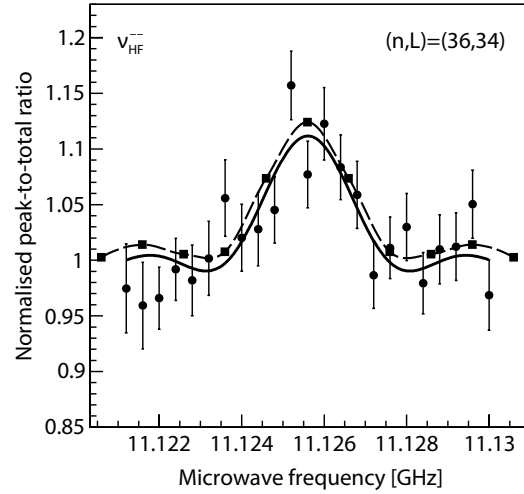


Figure 5: Scan over the microwave frequency for two of the four SSHF transitions for the $(n, L) = (36, 34)$ state of $\bar{p}^3\text{He}^+$, at a target pressure of 250 mbar. Each transition is fitted with Eq. 2. The frequencies of the measured transitions are 11.12559(14) GHz and 11.15839(18) GHz. The dashed curve shows a simulation using collision rates obtained from comparison between experiment and simulation.

385 mation that has been used for the calculations. The rel-
 386 ative error of the theoretical frequencies is estimated to
 387 be $\alpha^2 = 5 \times 10^{-5}$. The theoretical error for the frequency
 388 difference between theory and experiment would then
 389 be ~ 0.6 MHz. Together with the experimental error of
 390 ~ 0.2 MHz there is agreement between experiment and
 391 theory. Higher order correction terms need to be cal-
 392 culated to improve the theoretical results. The work on
 393 these calculations is in progress [21].

Table 1: The first experimental results for the ν_{HF}^{--} and ν_{HF}^{+-} in comparison with three-body QED calculations, where ν_{HF} denote the SSHF transition frequencies, δ_{exp} is the relative error of the measured frequencies and Γ the resonance line width. The theoretical precision is $\sim 5 \times 10^{-5}$.

	ν_{exp} (GHz)	δ_{exp} (ppm)	Γ (MHz)	Korobov [12, 21]	$\Delta\nu_{\text{th-exp}}$ (ppm)	Kino [11]	$\Delta\nu_{\text{th-exp}}$ (ppm)
ν_{HF}^{--} (GHz)	11.125 59(14)	13	2.08(22)	11.125 00(55)	-53	11.125 15(55)	-39
ν_{HF}^{+-} (GHz)	11.158 39(18)	16	1.92(19)	11.157 73(55)	-59	11.157 56(55)	-74
$\Delta\nu_{\text{HF}}^{\pm}$ (GHz)	0.03279(22)			0.0327219(16)			

A density dependent shift could also contribute to this deviation. The density dependence is found to be much smaller for the M1 transitions, the electron spin flip transitions induced by the microwave, than for the E1 transitions induced through laser stimulation [8]. For $\bar{\text{p}}^4\text{He}^+$ theoretical calculations of Grigory Korenman [22, 23] confirmed that the density dependence is very small. Also for $\bar{\text{p}}^3\text{He}^+$ theory predicts a collisional shift much smaller than our error bars [24].

The deviation between the experimental and theoretical values for the frequency difference $\Delta\nu_{\text{HF}}^{\pm} = \nu_{\text{HF}}^{+-} - \nu_{\text{HF}}^{--}$ between the two SSHF lines at 11 GHz is 68 kHz out of 32 MHz. This difference is important due to its proportionality to the magnetic moment of the antiproton. The error of the theoretical value for $\Delta\nu_{\text{HF}}^{\pm}$ is 1.6 kHz which is considerably smaller than the error of 220 kHz for the value obtained from the measured transitions. The reason is that in theory the splitting between the transition lines can be calculated directly and the errors are the same for all transitions within the hyperfine structure whereas the experimental value of the splitting is received from the difference of the single transition lines. Even though the experimental error is much larger than the theoretical one, there is agreement between theory and experiment within their errors.

6. Conclusions

We have reported on the first microwave spectroscopic measurement of the hyperfine structure of $\bar{\text{p}}^3\text{He}^+$. Two of the four favoured SSHF resonance transitions in $\bar{\text{p}}^3\text{He}^+$ were observed and are in agreement with theory [12] within the estimated theoretical error. Also the frequency difference $\Delta\nu_{\text{HF}}^{\pm}$ agrees with theoretical calculations. However, the experimental error for $\Delta\nu_{\text{HF}}^{\pm}$ is still very large compared to theory.

A systematic study of these transitions and improved statistics will allow a higher precision, in particular for the frequency difference between the SSHF transition frequencies, for which the experimental error is still considerably larger than the theoretical error. It is further planned to measure also the two SSHF transitions

at 16 GHz. The density dependence should be tested and different laser delay timings and microwave powers will be studied.

7. Acknowledgements

We are grateful to Dr. V. Korobov and Dr. G. Korenman for fruitful discussions on the theoretical framework. Further, we want to thank especially Ms. Silke Federmann and project student Mr. Mario Krenn for their help before and during the beamtime. This work has received funding from the Austrian Science Fund (FWF): [I-198-N20] as a joint FWF-RFBR (Russian Foundation for Basic Research) project, the Austrian Federal Ministry of Science and Research, the Japan Society for the Promotion of Science (JSPS), the Hungarian National Science Funds (OTKA K72172), the European Science Foundation (EURYI) and the Munich Advanced Photonics Cluster (MAP) of the Deutsche Forschungsgemeinschaft (DFG).

References

- [1] M. Iwasaki et al. Discovery of antiproton trapping by long-lived metastable states in liquid helium. *Phys. Rev. Lett.*, 67:1246–1249, 1991.
- [2] T. Yamazaki et al. Formation of long-lived gas-phase antiprotonic helium atoms and quenching by H_2 . *Nature*, 361:238–240, 1993.
- [3] T. Yamazaki et al. Antiprotonic helium. *Phys. Rep.*, 366:183–329, 2002.
- [4] R.S. Hayano et al. Antiprotonic helium and CPT invariance. *Reports on Progress in Physics*, 70(12):1995–2065, 2007.
- [5] T. Pask et al. A precise measurement of the antiprotonic helium hyperfine structure. *Phys. Lett. B*, 678(6):55–59, 2009.
- [6] A. Kreissl et al. Remesasurement of the magnetic moment of the antiproton. *Z. Phys. C*, 37:557–561, 1988.
- [7] E. Widmann et al. Hyperfine structure of antiprotonic helium revealed by a laser-microwave-laser resonance method. *Phys. Rev. Lett.*, 89:243402, 2002.
- [8] T. Pask et al. Collisional effects on the antiprotonic helium hyperfine structure measurement. *J. Phys. B: At. Mol. Opt. Phys.*, 41:081008, 2008.
- [9] D. Bakalov et al. Hyperfine structure of antiprotonic helium energy levels. *Phys. Rev. A*, 57:1662–1667, 1998.
- [10] V.I. Korobov et al. Fine and hyperfine structure of the (37,35) state of the $^4\text{He}^+\bar{\text{p}}$ atom. *J. Phys. B*, 34:519, 2001.

- [11] Y. Kino et al. High precision calculation of the fine and hyperfine structure of antiprotonic helium-3,4 atoms. *Hyperfine Interactions*, 146–147:331–336, 2003.
- [12] V.I. Korobov. Hyperfine structure of the metastable states of the ${}^3\text{He}^+\bar{p}$ atom. *Phys. Rev. A*, 73:022509, 2006.
- [13] M. Hori et al. Analog cherenkov detectors used in laser spectroscopy experiments on antiprotonic helium. *NIM A*, 496:102–122, 2003.
- [14] M. Hori et al. Primary populations of metastable antiprotonic ${}^4\text{He}$ and ${}^3\text{He}$ atoms. *Phys. Rev. Lett.*, 89:093401, 2002.
- [15] S. Maury et al. Status of the antiproton decelerator: AD. *Nucl. Phys. B (Proc. Suppl.)*, 56A:349–357, 1997.
- [16] J. Sakaguchi et al. Cryogenic tunable microwave cavity at 13 Ghz for hyperfine spectroscopy of antiprotonic helium. *NIM A*, 533:598–611, 2004.
- [17] O. Massiczek et al. Liquid helium free cryostat and hermetically sealed cryogenic microwave cavity for hyperfine structure spectroscopy of antiprotonic helium. *submitted*, 2011.
- [18] Ansoft. <http://www.ansoft.com/products/hf/hfss/>.
- [19] S. Flugge. Encyclopedia of physics. *Springer Verlag*, 1959.
- [20] T. Pask et al. Collisional effects on the measurement of the antiprotonic helium hyperfine structure. *Proceedings for the Pbar08 Conference on Cold Antimatter Plasmas and Application to Fundamental Physics (AIP) Japan, Okinawa*, 2008.
- [21] V.I. Korobov. *private communication*, 2010.
- [22] G.Y. Korenman et al. Coupled-channel analysis of collisional effects on HFS transitions in antiprotonic helium atoms. *Journal of Physics B: Atomic, Molecular and Optical Physics*, 39(6):1473–1484, 2006.
- [23] G.Y. Korenman et al. Collisional effects on HFS transitions of antiprotonic helium. *Hyperfine Interactions*, 194:29–35, 2009.
- [24] G.Y. Korenman. *private communication*, 2010.